

Supplementary Information: The impact of the interfacial thermal resistance on colloidal thermophoresis

Juan D. Olarte-Plata* and Fernando Bresme[†]
 Department of Chemistry, Imperial College London
 (Dated: June 11, 2024)

1. RELEVANT EQUATIONS FOR THE TEMPERATURE PROFILES AROUND COLLOIDS IN THE ABSENCE OF INTERFACIAL THERMAL CONDUCTANCE EFFECTS

For spherical colloids in an external temperature field ∇T , of magnitude $|\nabla T|$ in the \bar{x} direction, the temperature profile (in polar coordinates), far away from the particle is:

$$T^{ext} = T_0 + |\nabla T| \bar{x} = T_0 + |\nabla T| r \cos \theta \quad (1)$$

where T_0 is a reference temperature far from the colloid. See the main text for definitions of the symbols below. Near the colloid, the solvent, $T^s(R, \theta)$ and colloid, $T^c(R, \theta)$ profiles fulfill the boundary conditions:

$$T^s(R, \theta) = T^c(R, \theta) \quad (2)$$

$$\kappa^s \frac{\partial T^s(r, \theta)}{\partial r} \Big|_{r=R} = \kappa^c \frac{\partial T^c(r, \theta)}{\partial r} \Big|_{r=R} \quad (3)$$

Following references [1–3], the solution of the Laplace equation is:

$$T^s(r, \theta) = T_0 + |\nabla T| r \cos \theta \left[1 + \alpha \left(\frac{R}{r} \right)^3 \right] \quad (4)$$

$$T^c(r, \theta) = T_0 + |\nabla T| r \cos \theta [1 + \alpha] \quad (5)$$

where R is the colloid radius. An explicit equation for α follows from Eq. (3) above,

$$\alpha = \frac{\kappa^s - \kappa^c}{2\kappa^s + \kappa^c} \quad (6)$$

2. DERIVATION OF THE EQUATIONS DISCUSSED IN THE MAIN TEXT

We follow the approach of Würger to describe the relation between the surface stress and the Marangoni force for a freely drifting particle. The temperature gradient on the surface of the particle can be written as [4]:

$$\nabla_{\parallel} T = \left(\frac{1}{r} \frac{\partial T(r, \theta)}{\partial \theta} \right) \Big|_{r=R} = -|\nabla T| \sin \theta (1 + \alpha) \mathbf{t} \quad (7)$$

where \mathbf{t} is the tangential vector at the surface. The Marangoni force is given by [4]:

$$\nabla_{\parallel} \gamma = \gamma_T \nabla_{\parallel} T \quad (8)$$

where the Marangoni parameter is defined as the derivative of the interfacial free energy, γ , with respect to the temperature, $\gamma_T = d\gamma/dT$. The dissipative part of the stress tensor, σ' , is given by [4]:

$$\sigma'_{rr} = 2\eta \frac{\partial \hat{v}_r}{\partial r} \quad (9)$$

$$\sigma'_{r\theta} = \eta \left(\frac{1}{r} \frac{\partial \hat{v}_r}{\partial \theta} + \frac{\partial \hat{v}_\theta}{\partial r} - \frac{\hat{v}_\theta}{r} \right) \quad (10)$$

where η is the viscosity of the fluid. \hat{v}_r and \hat{v}_θ are the radial and tangential components of the fluid velocity field near the particle, in the particle frame of reference.

For a particle drifting with velocity $\mathbf{u} = u\hat{x}$ (due to the thermophoretic force), the solution to the Stokes equation for an incompressible fluid, $\eta \nabla^2 \hat{\mathbf{v}} = \nabla P$, can be written as [4]:

$$\hat{v}_r = -u \cos \theta \left(1 - \frac{R^3}{r^3} \right) \quad (11)$$

$$\hat{v}_\theta = u \sin \theta \left(1 + \frac{R^3}{2r^3} \right) \quad (12)$$

For this case, the tangential component of the stress tensor evaluated at the particle surface is:

$$\sigma'_{r\theta} \Big|_{r=R} = \frac{-3\eta u \sin \theta}{R} \quad (13)$$

The thermophoretic velocity of the particle can be found by balancing the tangential component of the stress tensor with the Marangoni force, $\sigma'_{\theta} \mathbf{t} = -\gamma_T \nabla_{\parallel} T$ [4], giving:

$$\frac{-3\eta u \sin \theta}{R} = \gamma_T |\nabla T| \sin \theta (1 + \alpha) \quad (14)$$

The drift velocity of the particle can thus be written as:

$$u = -\frac{\gamma_T R (1 + \alpha')}{3\eta} |\nabla T| \quad (15)$$

3. FORCES ON A FIXED PARTICLE

In our simulations, the translational motion of the nanoparticle is restrained in the middle plane between the hot and cold thermostats. This physical situation corresponds to that of a fixed particle and results in a velocity field distinctively different from the one obtained with the freely drifting particle. However, the corresponding friction force is the same except for a constant. Below, we derive the relevant equations for this case.

The total force on the particle is given by [5]

$$F_{tot} = \oint_S (-p \cos \theta + \sigma'_{rr} \cos \theta - \sigma'_{r\theta} \sin \theta) dA \quad (16)$$

where p is the pressure, and σ'_{ij} are components of the stress tensor.

The general solution for the fluid velocity around a spherical particle is given by [5]:

$$v_r = u_0 \cos \theta \left(1 - \frac{2a}{r} + \frac{2b}{r^3} \right) \quad (17)$$

$$v_\theta = -u_0 \sin \theta \left(1 - \frac{a}{r} - \frac{b}{r^3} \right) \quad (18)$$

where the constants a and b are determined from the boundary conditions. For instance, a freely drifting particle with *stick* boundary conditions implies that at $r = R$, $v_r = 0$ and $v_\theta = 0$. The solution is given by $a = 3R/4$ and $b = R^3/4$, which implies:

$$\hat{v}_r = u_0 \cos \theta \left(1 - \frac{3R}{2r} + \frac{R^3}{2r^3} \right) \quad (19)$$

$$\hat{v}_\theta = -u_0 \sin \theta \left(1 - \frac{3R}{4r} - \frac{R^3}{4r^3} \right) \quad (20)$$

For the fixed particle, the fluid velocity can be written as [6]:

$$v_r = u_0 \cos \theta \left(\frac{R}{r} - \frac{R^3}{r^3} \right) \quad (21)$$

$$v_\theta = -\frac{u_0 \sin \theta}{2} \left(\frac{R}{r} + \frac{R^3}{r^3} \right) \quad (22)$$

In this case, u_0 represents the velocity of the fluid at the particle's surface. With these expressions for the velocity field, we arrive to:

$$\sigma'_{rr}|_{r=R} = 4\eta \frac{u_0}{R} \cos \theta \quad (23)$$

$$\sigma'_{r\theta}|_{r=R} = 3\eta \frac{u_0}{R} \sin \theta \quad (24)$$

We note that the tangential stress, $\sigma'_{r\theta}$, has the same solution as the freely drifting particle with surface forces (see section 2 in the SI). This justifies using the approach proposed in

Ref. [4] when equating the tangential stress to the Marangoni force.

The corresponding contributions to the total force are given by:

$$F_{\sigma'_{rr}} = \frac{16\pi}{3} \eta R u_0 \quad (25)$$

$$F_{\sigma'_{r\theta}} = -8\pi \eta R u_0 \quad (26)$$

The pressure contribution to the total force can be found from the following expression [4]:

$$P = P_0 + 2\alpha \cos \theta \frac{\eta u_0 R}{r^2} \quad (27)$$

where $\alpha = 1/2$ corresponds to the solution for the fluid velocity field around the fixed particle. The pressure contribution to the total force thus reads:

$$F_P = -\frac{4\pi}{3} \eta R u_0 \quad (28)$$

The total force on the particle is thus given by:

$$F_{total} = F_{\sigma'_{rr}} + F_{\sigma'_{r\theta}} + F_P = -4\pi \eta R u_0 \quad (29)$$

From the previous equation, we note that the friction coefficient of the fixed particle with surface forces has a factor of 4π , as discussed in the main text.

4. SIMULATION DETAILS

The fluid, with reduced density $\rho = \rho_n \sigma^3 = 0.8$ (ρ_n is the number density in particles/m⁻³) was described using the WCA model, *i.e.* a Lennard-Jones 12-6 potential, $4\epsilon_s [(\sigma_s/r)^{12} - (\sigma_s/r)^6]$, with a cut-off radius corresponding to the minimum of the potential, *i.e.* $r_c = r_0 = 2^{1/6}\sigma$, with $\epsilon_s = 1.0$. σ is the diameter of the solvent and the particles inside the colloid. We used reduced units, $r = r_{SI}/\sigma$, $T = k_B T_K / \epsilon_s$, where r_{SI} is the distance in SI units, ϵ_s is the interaction strength between solvent particles and T_K the temperature in Kelvin. In these units the ITC is defined as, $G_{K,LJ} = G_K \sigma^2 / k_B \sqrt{m \sigma^2} / \epsilon_s$. All the solvent-particle interactions were computed using the WCA model. The interactions between the particles inside the colloids were described using a strongly attractive Lennard-Jones potential with interaction strength ϵ_s and a cut-off radius $r_c = 2.5\sigma$.

The simulations were run with a timestep $\delta t = 0.0025$ in Lennard Jones units, and using LAMMPS [7]. After 10^4 timesteps in the NVT ensemble with $T = 1.0$, the thermostats (see Figure S1) were activated. The first 10^5 timesteps were discarded before sampling for an additional 10^7 timesteps. The results reported in our work were obtained using 20 independent replicas, starting from random atomic velocities

and colloid orientations. To perform the simulations using the two setups (see Fig. S1), we generated cubic (*radial heat flux*) or rectangular (*external gradient*) simulation boxes with volume $V = (16a_0) \times (16a_0) \times (16a_0)$ or $V = (32a_0) \times (16a_0) \times (16a_0)$, where $a_0 = 2^{2/3}\sigma$ is the FCC lattice parameter of a solid with $\rho^* = 1.0$. To investigate finite-size effects in the computations of the Soret coefficient, we also simulated systems with $L_{y,z} = 20a_0$ for the *external gradient* set-up. In all cases, $L_x = 2L_{y,z}$. To set a temperature gradient, hot and cold thermostating regions were defined at the center and edges of the simulation box. The thermostating regions correspond to a spherical core, $r < 2.0\sigma$, and shell, $R > 9.7\sigma$ (*radial heat flux*), or rectangular slabs of width $4a_0$ (*external gradient*). Within these regions, the velocities of the fluid particles were rescaled to the target temperatures every 100 timesteps. The center-of-mass momentum was also removed with the same frequency to prevent a drift in the translational motion of the atoms. The *external gradient* configuration generates two temperature gradients in opposite directions. A spherical particle, cut from an FCC lattice with density $\rho = 1.0$ and radius $R = 5\sigma$, was placed in the center of each compartment and attached with harmonic potential, given by $U(r) = 0.5 k(r - r_0)^2$, with force constant $k = 10^3$. Snapshots of the simulation box and typical temperature profiles are shown in Fig. S1. All the visualizations were done using OVITO [8].

The temperature fields were calculated by dividing the simulation box in cubic voxels of volume $\sim (0.79\sigma)^3$, where the local temperature was sampled. To exploit the symmetry of the problem and improve sampling, the data was rebinned (using a weighted average) to (x, r) coordinates, where $r = \sqrt{y^2 + z^2}$. The bin size for the r coordinate was $\sim 0.56\sigma$. The contours were generated using a linear interpolation, with increasing levels of 0.05.

5. DENSITY PROFILES OF THE FLUID

Fig. S2 shows the radial density profile of the fluid as a function of radial distance to the center of geometry of the colloid and the colloid interaction strength, obtained under equilibrium conditions at $T = 2.0$. The results in Fig. S2 show that the colloid interactions do not impact the density profiles of the solvent surrounding the colloid.

6. CALCULATION OF THE COLLOID-SOLVENT INTERFACIAL THERMAL CONDUCTANCE, G_K

To compute the interfacial thermal conductance G_K we performed simulations targeting the highest and lowest interfacial temperatures obtained in the simulations of the Soret coefficient (see Fig. S1). Our simulations also consider the rectification of the G_K , namely, the solvent is hotter or colder on both sides of the colloid (see Fig. S1).

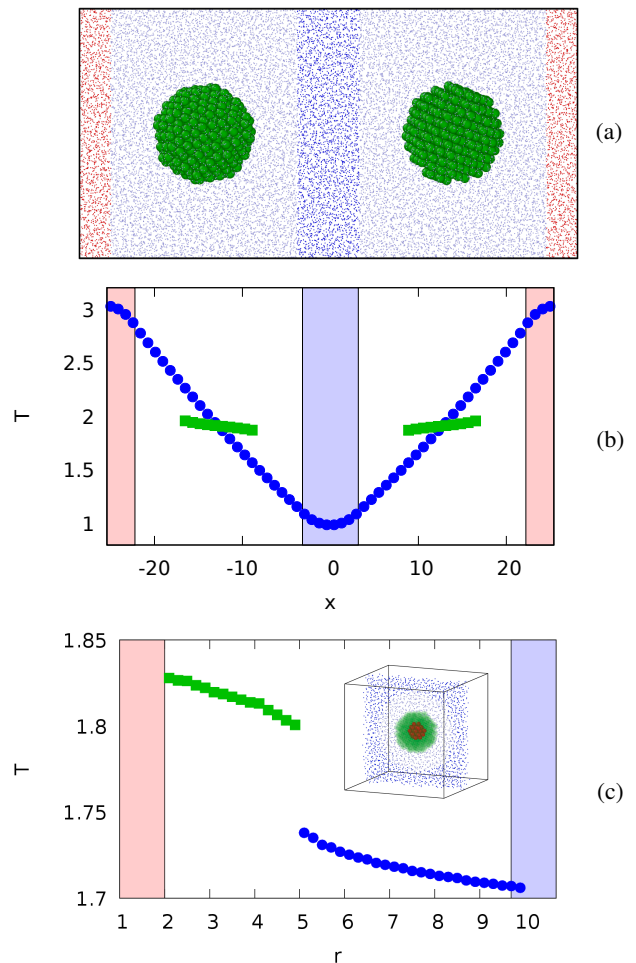


Fig. S1. (a) Snapshot of the simulation box in the *external gradient* set-up, showing the thermostating regions (red-hot, blue-cold). The solvent particles are represented as blue dots for visualization purposes, and the colloid as green spheres. (b) Temperature profile for a system with $\varepsilon_c/\varepsilon_s = 20$, showing the temperature of the fluid (blue circles) and the colloid (green squares). (c) Temperature profile for the *radial heat flux* system with $\varepsilon_c/\varepsilon_s = 20$, showing the temperature of the fluid (blue circles) and the spherical particle (green squares), and the corresponding temperature jump. The inset shows a snapshot of the simulation box, highlighting the thermostatted core (red) and the surrounding solvent (blue dots).

We now discuss the dependence of the Soret coefficient on the ITC. To address this point, we vary G_K , keeping the solvent-particle interaction strength constant and approximately the same interfacial temperature; hence, γ_T does not change with G_K . This notion is supported by the lack of dependence of the colloid solvation structure with ε_c (see Fig. S2). By modifying the colloid particle-particle interactions, we isolate G_K and surface tension effects. This leads to a systematic change of the colloid vibrational density of states (VDoS) relative to the VDoS of the solvent. By changing the overlap of the two VDoS we achieve higher or lower G_K , and we can systematically test Eq. (9) in the main paper. Figure S3 shows the impact of the ε_c on the overlapping of the col-

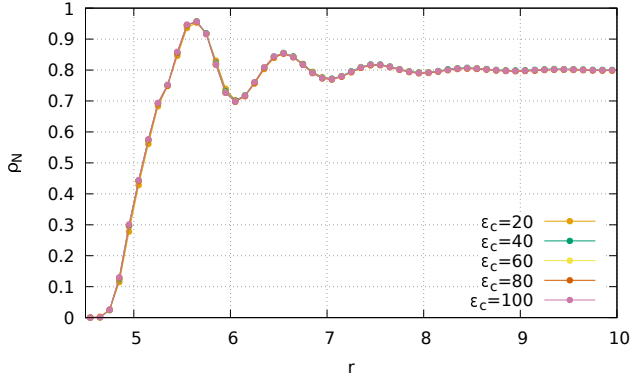


Fig. S2. Solvent radial density profiles around the colloid, as a function of the colloid interaction strength. The profiles were obtained at equilibrium conditions and $T = 2.0$.

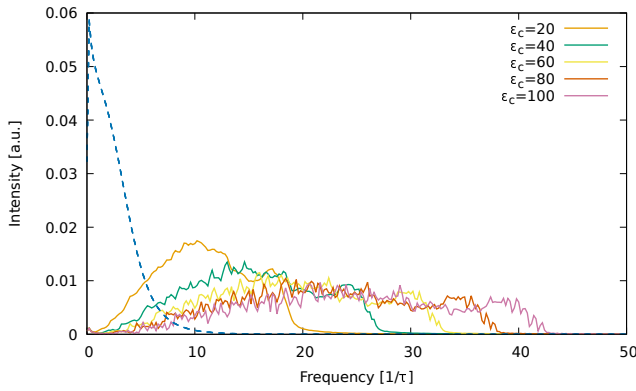


Fig. S3. (a) VDoS of the colloid and solvent as a function of ϵ_c . The fluid VDoS is represented with a blue dashed line.

loid and solvent Vibrational Density of States (VDoS). The ITC decreases with increasing ϵ_c due to a shift of the colloid VDoS to higher frequencies as ϵ_c increases (see Fig. S4).

The VDoS was computed as the Fourier transform of the velocity autocorrelation function for the fluid and solid particles:

$$VDoS_{j,k}(\omega) = \int_0^{\infty} \frac{\langle v_{j,k}(0)v_{j,k}(t) \rangle}{\langle v_{j,k}(0)v_{j,k}(0) \rangle} \exp(-2\pi i\omega t) dt \quad (30)$$

where $\langle v_{j,k}(0) \cdot v_{j,k}(t) \rangle$ is the velocity autocorrelation function of particle type j and component k . We used a simulation box equivalent to Fig. S1a with no temperature gradient and average temperature $T = 2.0$. The velocity autocorrelation function for fluid and colloid particles was calculated for 100 windows of 2500 timesteps each (using $\delta t = 0.001$) and averaged over ten replicas. All the colloid particles were included in the calculation.

We compute the interfacial thermal conductance of uniform nanoparticles as a function of their internal interaction strength using the *radial heat flux* simulation set-up (see Fig.

S1). The temperature of the colloid core is thermostatted to a target temperature $T_c = 1.9$. The temperature of the bulk solvent is varied between $T_s = 1.7$ and $T_s = 2.1$ to account for the colloid-solvent contact on the hot and cold regions (see Fig. S1). For the calculation of the temperature “jump”, we fitted the temperature profiles using the heat diffusion equation near the interfacial region (see Fig. S5). The range of radial distance for the colloid was restricted to $r_c^* = [4.0, 5.0]$, while for the solvent we used the interval $r_s = [5.0, 6.0]$.

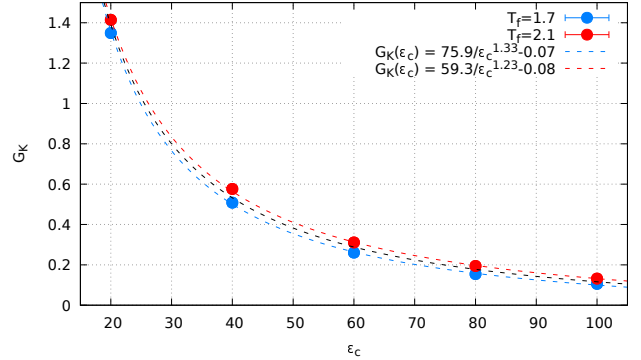


Fig. S4. Interfacial thermal conductance as a function of the colloid internal interaction strength for different bulk fluid temperatures. The dashed lines indicate fittings to a function of the form $G(\epsilon_c) = a/\epsilon_c^b + d$.

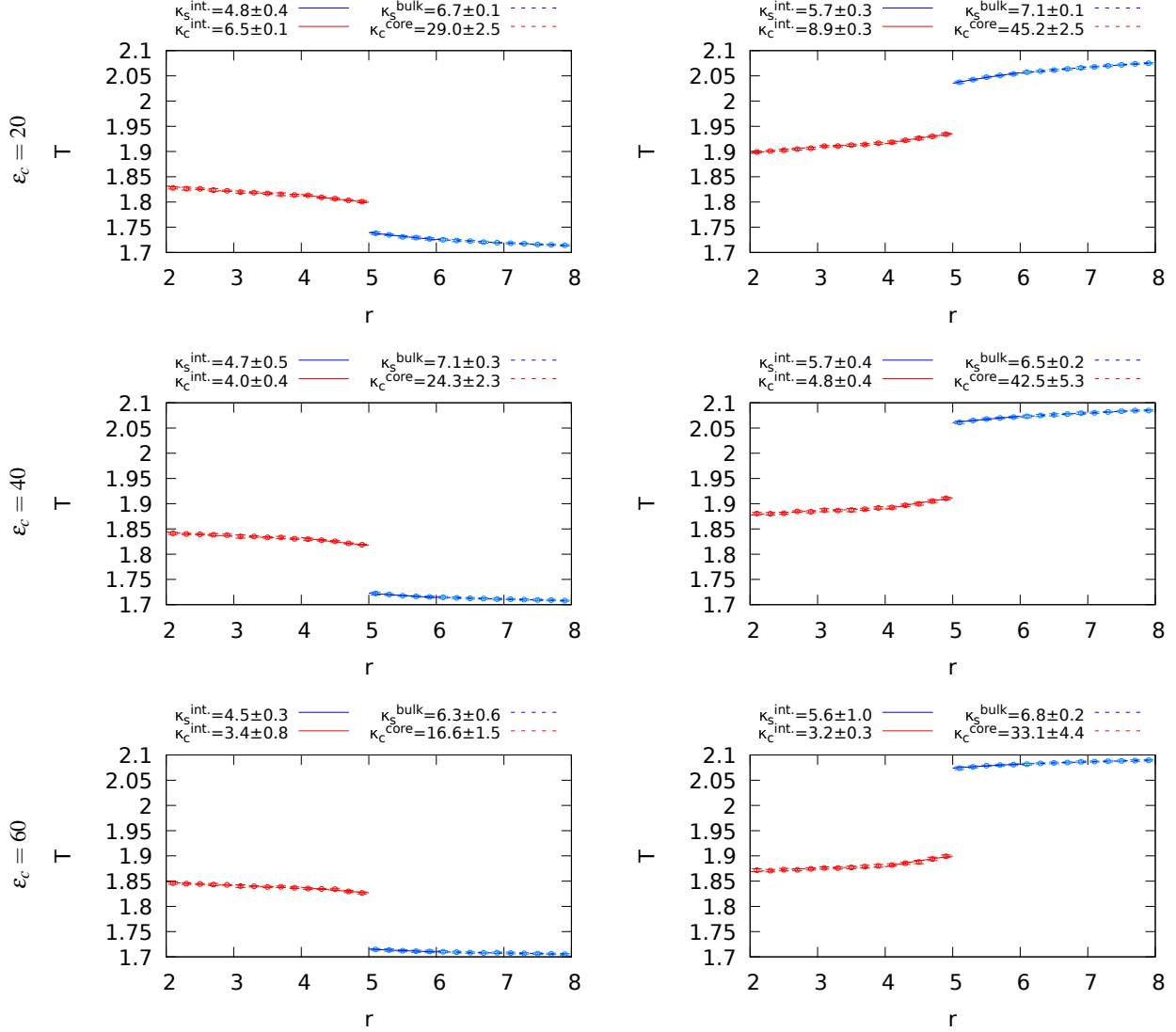


Fig. S5. Temperature profiles in the *radial heat flux* configuration, for different boundary conditions and colloid interaction strengths. The lines represent the fitting used to calculate the thermal gradient and thermal conductivities. κ_{α}^{β} refers to the colloid ($\alpha = c$) or solvent ($\alpha = s$) thermal conductivity obtained using the $\beta =$ “bulk” for the solvent, $\beta =$ “core” for the colloid or interfacial region $\beta =$ “int” for the solvent. Error bars represent the standard deviation calculated from the individual temperature profiles of 10 replicas.

6. THERMAL CONDUCTIVITY OF THE SOLVENT AND COLLOID

The thermal conductivity of the solvent was calculated using the *radial heat flux* simulation set-up (see Fig. S1). Due to the decreasing heat flux with increasing particle interaction strength, we focused on the range $\epsilon_c = 20 - 60$. Fig. S6 shows the thermal conductivity as a function of the fitting region and the boundary condition of the fluid. The thermal conductivity does not feature a significant variation with either temperature or particle interaction strength ϵ_c . Hence, to plot the theoretical curves in Fig. 3 in the main text, we used the thermal conductivities $\kappa_s^{bulk} = 6.87$ and $\kappa_s^{int.} = 5.16$ (see dashed horizontal lines in Fig. S6).

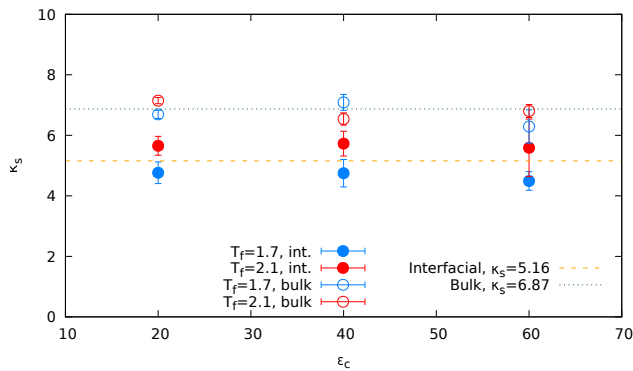


Fig. S6. Thermal conductivity of the solvent as a function of the colloid interaction strength and the temperature. The upper values were obtained using the temperature gradient in the bulk region and the lower values were obtained using the interfacial temperature gradient (see Fig. S5 for definitions of bulk and interfacial regions). Red and blue points represent the thermal conductivity at different temperatures, targeting the temperatures at the hot or cold side of the colloid surface (see Figure S1). The dashed horizontal lines represent the average thermal conductivities for each temperature and varying ϵ_c .

The thermal conductivity of the colloid (see Fig. S7) was calculated using the *radial heat flux* simulation set-up. We used Fourier's law by fitting the temperature gradient inside the colloid in an interval far from the colloid surface to avoid including interfacial effects (the interval $r_s = [2.0, 4.0]$).

Error bars for the thermal conductivities represent the asymptotic standard error from the fitting of the temperature profiles (and their associated standard deviations) shown in Fig. S5.

7. ESTIMATION OF THE EFFECTIVE THERMAL CONDUCTIVITIES OF FUNCTIONALIZED COLLOIDS

We used the following approach to estimate the effective thermal conductivity of the functionalized colloids discussed in Fig. 1c in the main paper. The effective thermal conductivity of the colloid, κ_{eff} , can be estimated using the model introduced by Hasselman and Johnson [9], which reduces to the

expression derived by Maxwell for infinite interfacial thermal conductance. As an example we consider here a gold colloid with $\kappa_{Au} \sim 300$ W/(K m), coated with an alkanethiol monolayer with $\kappa_m \sim 0.45$ W/(K m) [10] at ~ 300 K. The interfacial thermal conductance Au-monolayer interface is ~ 800 MW/(K m²)[10]. Following ref. [9] the effective thermal conductivity of the colloid is given by:

$$\kappa_{eff} = \kappa_m \frac{2 \left(\frac{\kappa_{Au}}{\kappa_m} - \frac{\kappa_{Au}}{RG_K} - 1 \right) V_{Au} + \frac{\kappa_{Au}}{\kappa_m} + \frac{2\kappa_{Au}}{RG_K} + 2}{\left(1 - \frac{\kappa_{Au}}{\kappa_m} + \frac{\kappa_{Au}}{RG_K} \right) V_{Au} + \frac{\kappa_{Au}}{\kappa_m} + \frac{2\kappa_{Au}}{RG_K} + 2} \quad (31)$$

where $V_{Au} = (R/(R+d))^3$ is the volume fraction of the gold particle with radius R , relative to the total volume of the colloid, defined by the radius $R+d$, where d is the thickness of the monolayer coating the gold core.

Considering a colloid of radius $R = 250$ nm and monolayers of thickness between 1 or 2 nm, we obtain the effective thermal conductivities 58.6 W/(K m) or 38.8 W/(K m), respectively. Ignoring the interfacial thermal conductance, $G_K \rightarrow \infty$, we find that the effective thermal conductivity is higher, 83.0 and 48.2 W/(K m) for monolayer thicknesses of 1 or 2 nm, respectively.

8. SORLET COEFFICIENT VS. INTERNAL INTERACTION STRENGTH AND SYSTEM SIZE

Fig. S8 shows the Soret coefficients obtained with the method discussed in section 2 above (see also discussion in the main paper pages 3 and 4). We considered different colloid interaction strengths as well as different system sizes. The Soret coefficient decreases with increasing system size (see Fig. S8 and also the discussion on the truncation of the hydrodynamic field in reference [11]).

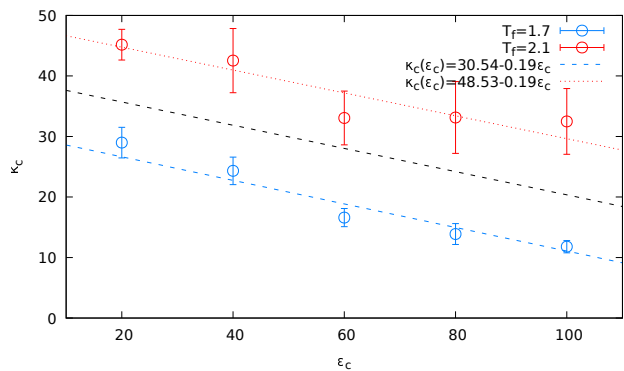


Fig. S7. Thermal conductivity of the colloid as a function of the colloid interaction strength for different temperatures. The dashed lines indicate fittings to a linear function. The black dashed lines represent the average of both high and low-temperature lines.

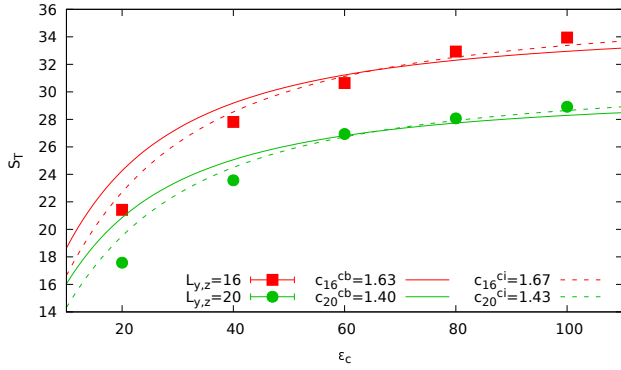


Fig. S8. Soret coefficient as a function of the particle interaction, ϵ_c , and system size. The symbols represent simulation results, and the lines fittings to the theoretical equations. See the discussion in the main text.

* j.olarte@imperial.ac.uk

† f.bresme@imperial.ac.uk

- [1] J. Giddings, P. M. Shinudu, and S. N. Semenov, *Journal of Colloid and Interface Science* **176**, 454 (1995).
- [2] T. Bickel, G. Zecua, and A. Würger, *Phys. Rev. E* **89**, 050303 (2014).
- [3] P. Gaspard and R. Kapral, *Journal of Statistical Mechanics: Theory and Experiment* **2019**, 074001 (2019).
- [4] A. Würger, *Phys. Rev. Lett.* **98**, 138301 (2007).
- [5] L. D. Landau and E. M. Lifshitz, *Fluid Mechanics, Second Edition: Volume 6 (Course of Theoretical Physics)*, 2nd ed., Course of theoretical physics / by L. D. Landau and E. M. Lifshitz, Vol. 6 (Butterworth-Heinemann, 1987).
- [6] J. Morthomas and A. Würger, *Phys. Rev. E* **81**, 051405 (2010).
- [7] S. Plimpton, *Journal of Computational Physics* **117**, 1 (1995).
- [8] A. Stukowski, *MODELLING AND SIMULATION IN MATERIALS SCIENCE AND ENGINEERING* **18** (2010), 10.1088/0965-0393/18/1/015012.
- [9] D. Hasselman and L. F. Johnson, *Journal of Composite Materials* **21**, 508 (1987), <https://doi.org/10.1177/002199838702100602>.
- [10] J. D. Olarte-Plata, J. Gabriel, P. Albella, and F. Bresme, *ACS Nano* **16**, 694 (2022).
- [11] F. Bresme, J. D. Olarte-Plata, A. Chapman, P. Albella, and C. Green, *Eur. Phys. J. E* **45**, 59 (2022).

The impact of the interfacial Kapitza resistance on colloidal thermophoresis

Juan D. Olarte-Plata* and Fernando Bresme[†]
Department of Chemistry, Imperial College London
(Dated: June 11, 2024)

Thermal gradients impart thermophoretic forces on colloidal particles, pushing colloids towards cold or hot regions, a phenomenon called thermophoresis. Current theoretical relate the Soret coefficient to local changes of the interfacial tension around colloid, which lead to fluid flow around the colloid surface. The Kapitza resistance, a key variable in the description of interfacial heat transport, is an experimentally accessible property that modifies interfacial thermal fields. Here, we introduce a theoretical approach that describes colloid thermophoretic forces by incorporating explicitly Kapitza resistance effects. Our formulation can be used to monitor the dependence of thermophoresis with the interfacial thermal resistance. We show that the Kapitza resistance modifies the thermal field around the colloids, and identify experimental conditions where the Kapitza resistance influences the thermophoretic forces. We validate our theoretical approach by implementing a non-equilibrium molecular dynamics model of a colloid suspended in a solvent.

Thermophoresis describes the motion of colloidal particles in solution. This physical effect was discovered by Ludwig and Soret in the 19th century using alkali halide aqueous solutions [1, 2]. Thermophoresis is a complex non-equilibrium phenomenon whose explanation has motivated experimental and theoretical works [3–15]. Following the behavior observed in thermodiffusion, colloids can feature thermophobic/philic behaviour at high/low temperatures. The phobic/philic transition temperature depends on the particle size [16] and screening length, in charged colloids [8]. Duhr and Braun introduced the idea of solvation entropy, connecting thermophoresis to interfacial properties [8]. Würger [6] developed a hydrodynamic theory where the colloid thermophoresis depends on the solvent and colloid thermal conductivities, the temperature derivative of the solvent-colloid surface energy (surface entropy) and the solvent viscosity. Arango-Restrepo and Rubi [17] derived an equation for the Soret coefficient using the Faxén theorem. Their equation does incorporate the derivative of the interfacial tension with temperature and the viscosities of the fluid and the particle.

Additional work on fluid-solid interfaces has been performed in the context of confined fluids and surfaces [18–21] focusing on the thermo-osmotic coefficient and following the non-equilibrium thermodynamics [22–25]. The fluid flow induced by thermo-osmosis emerges from stresses along a substrate fluid interface, and it is therefore an interfacial phenomenon. Evidence for fluid flow around nanoparticles has been provided recently using computer simulations [15].

At the colloid-fluid interface, thermodynamic and transport properties, such as density and thermal conductivity, feature abrupt changes. In the presence of a thermal gradient, these discontinuities give rise to the Kapitza resistance [26, 27] and an interfacial temperature “jump” that might influence the thermal field around a colloid, and potentially thermophoresis. The importance of the Kapitza resistance, or its inverse, the Interfacial Thermal Conductance (ITC), G_K , will depend on the magnitude of the conductances and, therefore, the colloid-solvent interfacial properties. High ITC will result in small temperature “jumps” at the colloid surface, but low ITC might lead to important differences in the interfacial temperatures

of the colloid and the solvent. To understand what constitutes high or low ITC, it is instructive to examine experimental studies of hydrophobic and hydrophilic interfaces [28]. The reported ITCs vary between $G_K = 50$ MW/(K m²), “low”, and 150 MW/(K m²), “high” ITC. Computer simulations of liquid-vapor interfaces reported even lower ITCs, ~ 1 MW/(K m²) [29], or higher ~ 200 -300 MW/(K m²) [30, 31] for gold-water interfaces. At low ITC, $G_K \sim 10$ MW/(K m²) measurable temperature differences between solvent and colloid, $\Delta T \sim 0.1$ -1 K, might appear for heat fluxes achievable in micro-fluidics ($\sim 10^6$ K/m) [8] or plasmonic heating (10^8 K/m) [32].

Here we incorporate ITC effects in the theory of thermophoresis. Hence, we incorporate in the theory an experimental variable that is becoming increasingly important in the design of thermal management devices, as well as on the interpretation of nanoscale heat transfer experiments. We show that the ITC modifies the temperature field around a colloid, and the thermophoretic force, particularly at low ITCs. We corroborate the general predictions of the theory using non-equilibrium molecular dynamics simulations.

THEORETICAL MODEL

Several authors [6, 33–35] derived equations for the Soret coefficient of spherical colloids by considering the deformation of the temperature field and the ensuing interfacial tension gradient around the colloid, which leads to a Marangoni force. The deformation of the temperature field emerges from the contrast of thermal conductivities of the solvent, κ^s , and that of the colloid, κ^c . For a spherical colloid immersed in an external temperature field ∇T , of magnitude $|\nabla T|$ in the \vec{x} direction, the temperature profile (in polar coordinates), far away from the particle is:

$$T^{ext} = T_0 + |\nabla T| \vec{x} = T_0 + |\nabla T| r \cos \theta \quad (1)$$

where T_0 is a reference temperature far from the colloid. Near

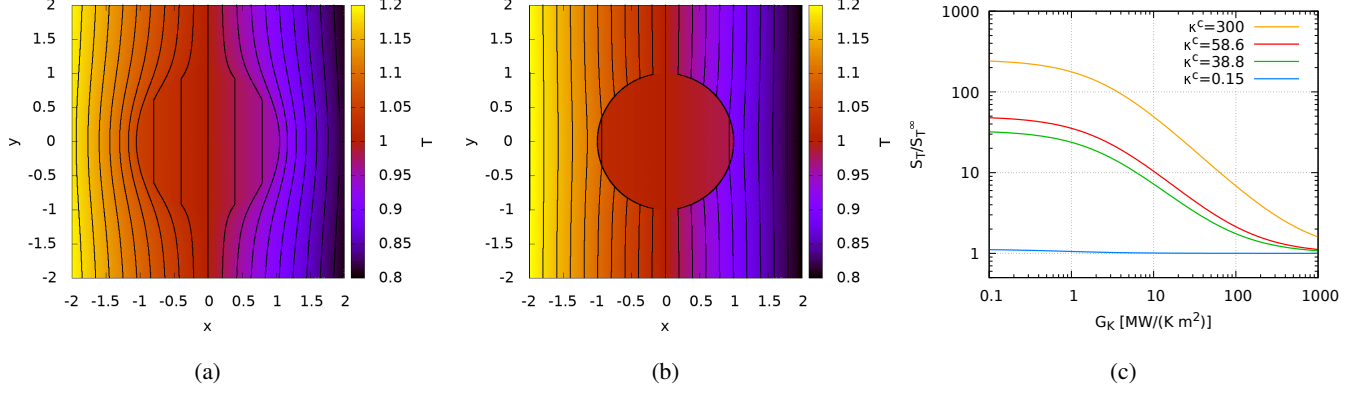


FIG. 1. Temperature field around a spherical colloid of radius $R = 1.0$, without (a) and with (b) ITC effects. The results in (a) were obtained using Eqs. (4) and (5) in the SI, and those in (b) with Eqs. (9) and (10). We used $\kappa^s = 1.0$, $\kappa^c = 4.0$, $G_K = 1.0$, average temperature $T_0 = 1$, and $|\nabla T| = 0.1$. These reduced units are compatible with a colloid of radius 250 nm in water, $\kappa^c/\kappa^s = 4$ ($\kappa^s = 0.6 \text{ W}/(\text{K m})$), $G_K \sim 3 \text{ MW}/(\text{K m}^2)$. (c) Predicted S_T as a function of G_K , for different κ^c (in units of $\text{W}/(\text{K m})$) and $\kappa^s = 0.6 \text{ W}/(\text{K m})$. The lines represent results obtained with Eq. (17). S_T has been divided by the Soret coefficient, S_T^∞ at $G_K \rightarrow \infty$, *i.e.* when the ITC effects are neglected. The results for S_T^∞ were obtained using Eq. (15) and α (Eq. (6) in the SI) instead of α' .

the colloid, the solvent, $T^s(R, \theta)$ and colloid, $T^c(R, \theta)$ temperature profiles fulfill the boundary conditions:

$$T^s(R, \theta) = T^c(R, \theta) \quad (2)$$

$$\kappa^s \frac{\partial T^s(r, \theta)}{\partial r} \Big|_{r=R} = \kappa^c \frac{\partial T^c(r, \theta)}{\partial r} \Big|_{r=R} \quad (3)$$

Following [33–35] the solution of the Laplace equation is:

$$T^s(r, \theta) = T_0 + |\nabla T| r \cos \theta \left[1 + \alpha \left(\frac{R}{r} \right)^3 \right] \quad (4)$$

$$T^c(r, \theta) = T_0 + |\nabla T| r \cos \theta [1 + \alpha] \quad (5)$$

where R is the colloid radius. The parameter α quantifies the thermal conductivity contrast between the colloid and the fluid. An explicit equation for α follows from the boundary condition in Eq. (3),

$$\alpha = \frac{\kappa^s - \kappa^c}{2\kappa^s + \kappa^c} \quad (6)$$

The solvent-colloid interface results in an interfacial thermal conductance that modifies the boundary conditions given by Eqs. (2) and (3), as the temperature features a discontinuous jump, $\Delta T = \frac{J_q}{G_K}$, defined by the heat flux, J_q , and the interfacial thermal conductance, G_K . The new boundary conditions, including G_K are,

$$T^{ls}(R, \theta) - \frac{\kappa^s}{G_K} \frac{\partial T^{ls}(r, \theta)}{\partial r} \Big|_{r=R} = T^{lc}(R, \theta) \quad (7)$$

$$\kappa^s \frac{\partial T^{ls}(r, \theta)}{\partial r} \Big|_{r=R} = \kappa^c \frac{\partial T^{lc}(r, \theta)}{\partial r} \Big|_{r=R} \quad (8)$$

where the prime indicates the equations include the interfacial thermal conductance effect. The solution of Eqs. (7) and (8) gives the corresponding temperature profiles,

$$T^{ls}(r, \theta) = T_0 + |\nabla T| r \cos \theta \left[1 + \alpha' \left(\frac{R}{r} \right)^3 \right] \quad (9)$$

$$T^{lc}(r, \theta) = T_0 + |\nabla T| r \cos \theta [1 + \alpha' + \beta'] \quad (10)$$

where α' and β' are

$$\alpha' = \frac{\kappa^s - \kappa^c(1 + \beta')}{2\kappa^s + \kappa^c} \quad (11)$$

$$\beta' = \frac{-3\kappa^s \kappa^c}{G_K R (2\kappa^s + \kappa^c) + 2\kappa^s \kappa^c}. \quad (12)$$

For $G_K \rightarrow \infty$, $\beta' \rightarrow 0$ and we recover Eqs. (4) and (5). We note that Eqs. (9) and (10) agree with those derived in reference [36] to obtain the effective thermal conductivity of composites.

Fig. 1 shows the temperature profiles around the colloid with and without interfacial thermal conductance effects. The ITC has a significant impact on the temperature field, and the temperature profile features a discontinuity for the solution that includes the ITC effects. Although the temperature field appears less deformed in the vicinity of the colloid, the ITC leads to different thermal fields far from the colloid surface. The changes in the thermal field influence the thermophoretic force, thermophoretic velocity, and ultimately the Soret coefficient. We now follow the approach introduced in reference [6] to address these changes. We obtain the thermophoretic velocity by considering the surface stress around the colloid. The

drift velocity of the particle is given by (see section 1 in the SI for a derivation of the equations given below):

$$u = -\frac{\gamma_T R(1 + \alpha')}{3\eta} |\nabla T| \quad (13)$$

where η is the solvent viscosity and $\gamma_T = d\gamma/dT$ quantifies the change of the interfacial tension, γ , with temperature. In this theory, the thermophoretic force is a Marangoni force emerging from the surface stress around the colloid due to the temperature gradient. The thermal diffusion coefficient is defined by the factor in front of the thermal gradient in Eq. (13)

$$D_T = \frac{\gamma_T R(1 + \alpha')}{3\eta} \quad (14)$$

which again reduces to the equations reported in previous work [6] when G_K is neglected. The Soret coefficient is given by $S_T = D_T/D$, where D is the interdiffusion coefficient approximated for highly diluted suspensions by the colloid diffusion coefficient. For a spherical colloid, $D = k_B T / (\xi \pi \eta R)$, where ξ is a numerical parameter accounting for the boundary conditions. The Soret coefficient is given by:

$$S_T = 4\pi R^2 \frac{(1 + \alpha') \gamma_T}{3k_B T} + \frac{1}{T}, \quad (15)$$

where the α' parameter considers the different thermal conductivities of the solvent and colloid and the interfacial thermal conductance. The second term of Eq. (15) represents the ideal contribution to the Soret coefficient. The origin of the factor “4” in Eq. (15) is justified in the derivation included in the SI (see section 2).

The scaling of the Soret coefficient with the square of the colloid radius (R^2) and the inverse of the temperature is consistent with previous computations of Soret coefficients [37]. However, α' introduces an additional dependence on the colloid radius through Eq. (12). The solution, including G_K for the solvent and colloid temperature profiles, results in a larger deformation of the temperature field far from the particle (see Figures 1a,b) and a temperature discontinuity at the colloid surface. Based on Eq. (12), we expect that the impact of the interfacial thermal conductance on the Soret coefficient will be stronger when the thermal conductivities of the solvent and the colloid are very different. Figure 1c illustrates the impact of G_K on the predicted Soret coefficient for a colloid of radius $R = 250$ nm immersed in water with $\kappa^s = 0.6$ W/(K m). For the colloid, we consider a range of thermal conductivities, $\kappa^c = 0.15 \dots 300$ W/(K m). The intermediate thermal conductivities, 58.6 and 38.8 W/(K m), might be representative of the thermal conductivity of a gold nanoparticle coated with a 1 nm or 2 nm alkane passivating layer, with a thermal conductivity for the layer of 0.45 W/(K m)[38] (see SI section 7, for more details). We also consider the thermal conductivity of a colloid made of polystyrene with $\kappa^c = 0.15$ W/(K m) as well as high thermal conductivity, of the order of that of bulk

gold, $\kappa^c = 300$ W/(K m). The range of ITCs represented in Figure 1c, covers values corresponding to liquid-vapour interfaces (1 MW/(K m²) [39], and hydrophobic and hydrophilic self assembled monolayers (50-1000 MW/(K m²)) [28, 38]. For similar solvent and colloid thermal conductivities, the impact of G_K is relatively small, and the results converge to the previous solution that assumes $G_K \rightarrow \infty$. The convergence is much slower when κ^s and κ^c are very different. Moreover, at low G_K , the difference in the Soret coefficient is significant, even for interfacial thermal conductances corresponding to hydrophobic layers, ~ 50 MW/(K m²). In summary, our results show that low ITCs can significantly enhance the Soret coefficient when the thermal conductivity of the colloid is much higher than the thermal conductivity of the solvent.

We have shown that the Soret coefficient is proportional to the parameter $1 + \alpha'$. We now extend the analysis of the dependence of this parameter on the thermal transport coefficients of the system by introducing the dimensionless quantities $\lambda = \kappa^s / \kappa^c$ and $\varepsilon = G_K R / \kappa^s$. The first quantity is simply the ratio between the thermal conductivities of the solvent and the colloid, while the latter relates the interfacial thermal resistance of the interface with that of the fluid. Using these definitions, we can express the parameter $1 + \alpha'$ as:

$$1 + \alpha' = \frac{3\lambda + \frac{3}{\varepsilon(2\lambda + 1) + 2}}{2\lambda + 1} \quad (16)$$

The solution when $\varepsilon \rightarrow \infty$ converges to $1 + \alpha = 3\lambda / (2\lambda + 1) = 3\kappa^s / (2\kappa^s + \kappa^c)$. The ratio between the solutions with and without considering the ITC can be written as:

$$\frac{S_T}{S_T^\infty} = \frac{1 + \alpha'}{1 + \alpha} = 1 + \frac{1}{\lambda \varepsilon (2\lambda + 1) + \lambda} \quad (17)$$

where S_T^∞ is the Soret coefficient for $G_K \rightarrow \infty$.

Test of the theoretical model using computer simulations

We test the theoretical predictions using computer simulations of a colloid immersed in a WCA solvent at reduced density, $\rho = 0.8$ (see SI for details on the simulation setup and model). We also use the WCA potential to model the fluid-colloid interactions. The interactions inside the colloid are described with the spherically truncated and shifted Lennard-Jones potential with interaction strengths varying between $\varepsilon_c / \varepsilon_s = 20 \dots 100$, where ε_s and ε_c are the interaction strengths between solvent particles and the particles in the colloid, respectively.

We used two simulation set-ups to test the theoretical predictions. G_K , κ^s and κ^c were obtained using a *radial heat flux* simulation set-up (see Fig. S1-c). The deformation of the temperature field due to the presence of the spherical particle was studied using an *external gradient* set-up (see Fig.S1-a,b).

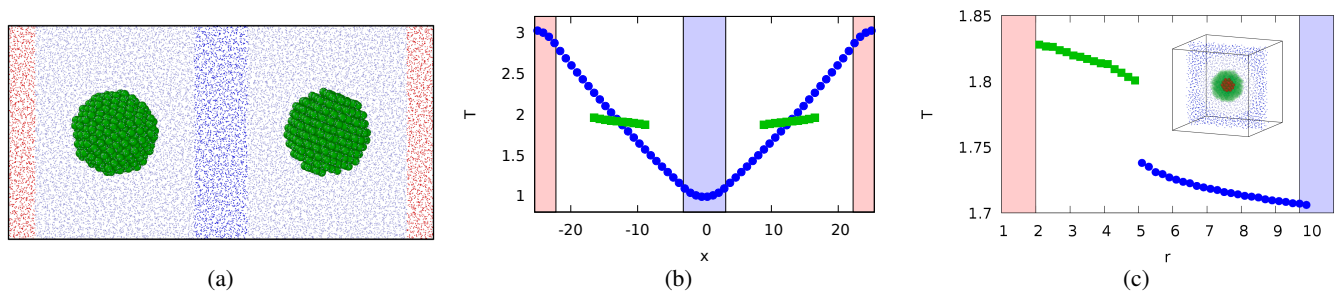


FIG. 2. (a) Snapshot of the simulation box in the *external gradient* set-up, showing the thermostating regions (red-hot, blue-cold). The solvent particles are represented as blue dots for visualization purposes, and the colloid as green spheres. (b) Temperature profile for a system with $\epsilon_c/\epsilon_s = 20$, showing the temperature of the fluid (blue circles) and the colloid (green squares). (c) Temperature profile for the *radial heat flux* system with $\epsilon_c/\epsilon_s = 20$, showing the temperature of the fluid (blue circles) and the spherical particle (green squares), and the corresponding temperature jump. The inset shows a snapshot of the simulation box, highlighting the thermostatted core (red) and the surrounding solvent (blue dots).

In both set-ups, the thermal gradients are simulated explicitly by setting hot and cold boundaries (see Fig. S1). The *external gradient* set-up was also employed to compute the thermal conductivity of the solvent and the Soret coefficient by computing the thermophoretic force associated with the displacement of the colloids attached with a harmonic spring to the geometric centre of the reservoirs shown in Fig. S1-a,b (see e.g. ref.[15] for details on this method). The thermal conductivity and ITC were obtained from the heat flux using Fourier’s law, $J_q = -\kappa \nabla T$ and the Kapitza relation, $J_q = G_K \Delta T$, where ∇T is the thermal gradient, and ΔT the temperature “jump” at the colloid-solvent interface (see Fig. S1-c). Further simulation details are provided in the SI (see section 4).

First, we compare the predicted field around the spherical colloid against the simulated data using Eqs. (4) and (5) in the SI, replacing α by α' to include ITC effects (see SI for details on the computation of the temperature field using NEMD simulations). We find good agreement between the predictions of the analytical solution and the NEMD results (see Fig. 3), with some deviations at the colloid surface, connected to the granularity of the colloid surface. Away from the interfacial region, the agreement of the temperature field is good, supporting the accuracy of Eqs. (4) and (5) in the SI.

The impact of the ITC on the temperature field is also evident (c.f. Figs.3-a, b and c). The field features stronger deformation with decreasing ITC, evident at distances > 5 solvent molecular diameters. Analytical and simulation results indicate that ITC effects are needed to describe temperature fields around colloids.

We now discuss the theoretical predictions and simulated S_T . The S_T computation using the setup in Fig.S1-a involves restraining the translational motion of the colloid with a spring, which results in a hydrodynamic flow[15, 40] around the colloid and a system size-dependent S_T . For a given system size, the S_T is of the same order as the one obtained from the thermophoretic velocity of a freely drifting particle [11]. We computed S_T for system sizes $L_{y,z} = 16$ and 20. To test the numerical results against Eq. (15), we used the colloid and solvent thermal conductivities corresponding to the bulk re-

gions (see section 6 in the SI), the ITC obtained with the radial heat flux method (see Fig.S1-c), and the colloid radius, $R = 5$. We set a constant fitting parameter in Eq. (15), $c = 4\gamma_T \chi_{L_{y,z}}$, where $\chi_{L_{y,z}}$ takes into account the finite size of the simulation box and its impact on S_T .

Figure 4 shows the dependence of the simulated Soret coefficients with G_K . The general dependence agrees with the theoretical results predicted by Eq. (15) and those shown in Figure 1c, namely, S_T decreases with increasing G_K . We find that Eq. (15) reproduces the trends of the simulated S_T , but some deviations are evident at large G_K . We note that we used the bulk solvent thermal conductivities in the theoretical calculation. However, the density of the solvent next to the colloid differs significantly from the bulk density (see Fig. S2). Hence, we recalculated the solvent thermal conductivity, including only the region within one molecular diameter from the colloid surface. The thermal conductivity of this layer is lower than the bulk one (see Fig. S6 in the SI), and it leads to a better agreement between the simulation data and the theory (see Fig. 4).

FINAL REMARKS

We have extended previous theories of the Soret effect[6, 33–35], and presented the analytical solution to the temperature field around a spherical colloid, including the Kapitza resistance, to account for the temperature discontinuity at the colloid-solvent interface. In our formulation, the Soret coefficient varies with the deformation of the thermal field around the colloid, the thermal conductivities of colloid and solvent, and the ITC. The resulting equation includes corrected thermal conductivity terms to account for the ITC, G_K . We show that the Soret coefficient depends strongly on ITC, for high colloid thermal conductivities ($\kappa_c \gg \kappa_s$), when $G_K < 100 - 300 \text{ W}/(\text{K m}^2)$. These conditions can be found in gold nanoparticle suspensions. For $\kappa^c \sim \kappa^s$ (e.g. polymer nanoparticles), the impact of G_K is small, and for $G_K \rightarrow \infty$, we recover previous theories, which ignored G_K effects. We

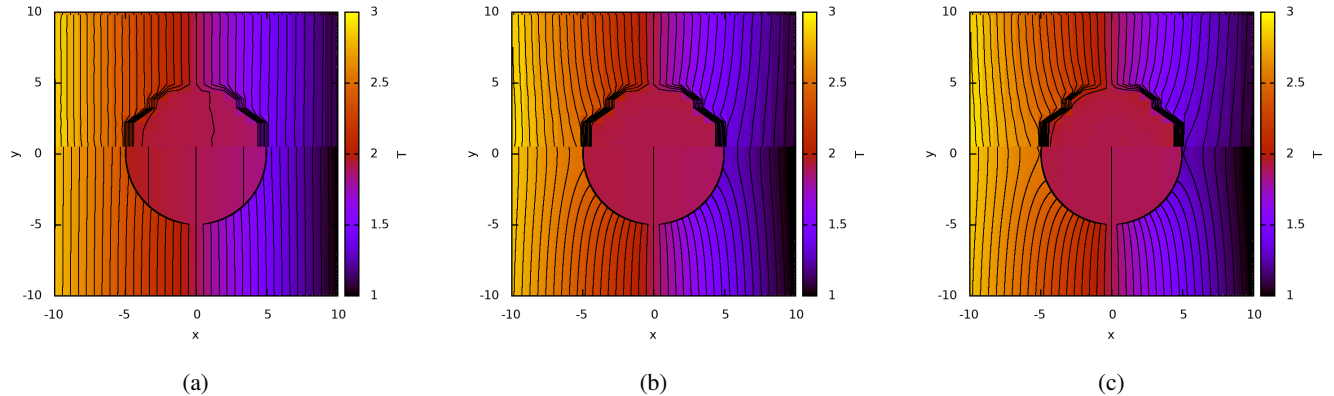


FIG. 3. Overlay of the NEMD simulation ($y > 0$) and analytical results ($y < 0$), for $\varepsilon_c/\varepsilon_s = 20, 60, 100$ corresponding to three ITCs, $G_{K,LJ} = 1.4$ (a), 0.3 (b) and 0.11 (in Lennard Jones units, see SI). (c), and colloid thermal conductivities of $\kappa^c = 36$ (a), $\kappa^c = 28$ (b) and $\kappa^c = 20.5$ (c) (see SI for details regarding calculations of the thermal conductivities). All the results were obtained using $\kappa^s = 6.87$, $T_0 = 1.9$ and $|\nabla T| = 0.09$.

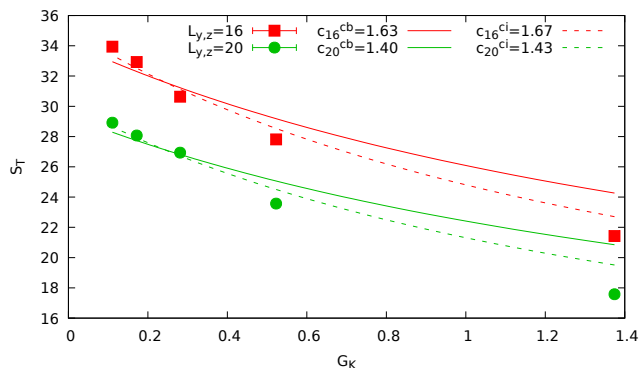


FIG. 4. Soret coefficient as a function of G_K and system size. The solid lines represent fittings using the bulk fluid thermal conductivity (fitting parameter denoted by cb). The dashed lines represent fittings to Eq. (15) using the fluid interfacial thermal conductivity (fitting parameter denoted by ci). In both cases, the colloid core thermal conductivity was used.

have verified the analytical equations using non-equilibrium molecular dynamics simulations of coarse-grained models of colloids immersed in a solvent. The simulated temperature fields agree with the “continuum” theory, and the Soret coefficient varies with G_K as predicted theoretically.

Our work highlights the importance of non-equilibrium effects associated to explicit temperature gradients. Recently [41] it was suggested that thermophoresis is dominated by fluctuations at Peclet number (small thermal gradients), $Pe = RS_T \nabla T < 1$, and by non-equilibrium transport for $Pe > 1$. The system investigated here is consistent with the $Pe > 1$ regime, where interfacial thermal gradients determine the thermophoretic motion. Furthermore, we find this non-equilibrium transport to dominate in a situation where the colloid is not much larger than the boundary layer.

Our work highlights the importance of the ITC in the

thermophoresis of colloidal particles. This contribution has been ignored before, but as demonstrated here, it influences the temperature field around colloids and the thermophoretic force. We anticipate that the ideas presented here will be helpful in advancing the description of thermophoresis, a very complex non-equilibrium coupling effect with potential applications to colloidal trapping, nanofluidics, and the design of analytical devices.

We thank the Leverhulme Trust for grant RPG-2018-384 and the Imperial College High-Performance Computing Service for providing computational resources.

References

- * j.olarte@imperial.ac.uk
- † f.bresme@imperial.ac.uk
- [1] C. Ludwig, Sitzber. Akad. Wiss. Wien Math.-naturw. Kl. **20**, 539 (1856).
- [2] C. Soret, Arch. Sci. Phys. Nat. Geneve **2**, 48 (1879).
- [3] S. Wiegand, Thermal diffusion in liquid mixtures and polymer solutions, *Journal of Physics: Condensed Matter* **16**, R357 (2004).
- [4] S. Semenov and M. Schimpf, Thermophoresis of dissolved molecules and polymers: Consideration of the temperature-induced macroscopic pressure gradient, *Phys. Rev. E* **69**, 011201 (2004).
- [5] S. A. Putnam and D. G. Cahill, Transport of nanoscale latex spheres in a temperature gradient, *Langmuir* **21**, 5317 (2005).
- [6] A. Würger, Thermophoresis in colloidal suspensions driven by marangoni forces, *Phys. Rev. Lett.* **98**, 138301 (2007).
- [7] R. Piazza and A. Parola, Thermophoresis in colloidal suspensions, *Journal of Physics: Condensed Matter* **20**, 153102 (2008).
- [8] S. Duhr and D. Braun, Why molecules move along a temperature gradient, *Proceedings of the Na-*

- tional Academy of Sciences **103**, 19678 (2006), <https://www.pnas.org/content/103/52/19678.full.pdf>.
- [9] G. Galliero and S. Volz, Thermodiffusion in model nanofluids by molecular dynamics simulations, *The Journal of Chemical Physics* **128**, 064505 (2008), <https://doi.org/10.1063/1.2834545>.
- [10] H. Brenner, Self-thermophoresis and thermal self-diffusion in liquids and gases, *Phys. Rev. E* **82**, 036325 (2010).
- [11] D. Lüsebrink, M. Yang, and M. Ripoll, Thermophoresis of colloids by mesoscale simulations, *Journal of Physics: Condensed Matter* **24**, 284132 (2012).
- [12] J. Burelbach, M. Zupkauskas, R. Lamboll, Y. Lan, and E. Eiser, Colloidal motion under the action of a thermophoretic force, *The Journal of Chemical Physics* **147**, 094906 (2017), <https://doi.org/10.1063/1.5001023>.
- [13] A. Arango-Restrepo and J. M. Rubi, The soret coefficient from the faxén theorem for a particle moving in a fluid under a temperature gradient, *The European Physical Journal E* **42**, 55 (2019).
- [14] J. D. Olarte-Plata and F. Bresme, Theoretical description of the thermomolecular orientation of anisotropic colloids, *Phys. Chem. Chem. Phys.* **21**, 1131 (2019).
- [15] F. Bresme, J. D. Olarte-Plata, A. Chapman, P. Albella, and C. Green, Thermophoresis and thermal orientation of janus nanoparticles in thermal fields, *Eur. Phys. J. E* **45**, 59 (2022).
- [16] M. Braibanti, D. Vigolo, and R. Piazza, Does thermophoretic mobility depend on particle size?, *Phys. Rev. Lett.* **100**, 108303 (2008).
- [17] Arango-Restrepo, Andrés and Rubi, J. Miguel, The soret coefficient from the faxén theorem for a particle moving in a fluid under a temperature gradient, *Eur. Phys. J. E* **42**, 55 (2019).
- [18] L. Fu, S. Merabia, and L. Joly, What controls thermo-osmosis? molecular simulations show the critical role of interfacial hydrodynamics, *Phys. Rev. Lett.* **119**, 214501 (2017).
- [19] R. Ganti, Y. Liu, and D. Frenkel, Molecular simulation of thermo-osmotic slip, *Phys. Rev. Lett.* **119**, 038002 (2017).
- [20] W. Q. Chen, M. Sedighi, and A. P. Jivkov, Thermo-osmosis in hydrophilic nanochannels: mechanism and size effect, *Nanoscale* **13**, 1696 (2021).
- [21] B. Hafskjold, D. Bedeaux, S. Kjelstrup, and Ø. Wilhelmsen, Soret separation and thermo-osmosis in porous media, *The European Physical Journal E* **45**, 41 (2022).
- [22] B. Derjaguin and G. Sidorenkov, On thermo-osmosis of liquid in porous glass, *CR Acad. Sci. URSS, Moscow* **32**, 622 (1941).
- [23] B. Derjaguin, N. Churaev, and V. Muller, *Surface Forces* (Plenum, New York, 1987).
- [24] J. L. Anderson, Colloid transport by interfacial forces, *Annual Review of Fluid Mechanics* **21**, 61 (1989).
- [25] S. Kjelstrup and D. Bedeaux, *Non-Equilibrium thermodynamics of heterogeneous systems* (World Scientific, Hackensack, 2008).
- [26] P. L. Kapitza, Heat transfer and superfluidity of helium ii, *Phys. Rev.* **60**, 354 (1941).
- [27] E. T. Swartz and R. O. Pohl, Thermal boundary resistance, *Rev. Mod. Phys.* **61**, 605 (1989).
- [28] Z. Ge, D. G. Cahill, and P. V. Braun, Thermal conductance of hydrophilic and hydrophobic interfaces, *Phys. Rev. Lett.* **96**, 186101 (2006).
- [29] J.-M. Simon, S. Kjelstrup, D. Bedeaux, and B. Hafskjold, Thermal flux through a surface of n-octane. a non-equilibrium molecular dynamics study, *The Journal of Physical Chemistry B* **108**, 7186 (2004).
- [30] H. Bhattarai, K. E. Newman, and J. D. Gezelter, The role of polarizability in the interfacial thermal conductance at the gold-water interface, *The Journal of Chemical Physics* **153**, 204703 (2020), <https://doi.org/10.1063/5.0027847>.
- [31] J. D. Olarte-Plata and F. Bresme, Thermal conductance of the water-gold interface: The impact of the treatment of surface polarization in non-equilibrium molecular simulations, *The Journal of Chemical Physics* **156**, 204701 (2022), <https://doi.org/10.1063/5.0090983>.
- [32] A. O. Govorov, W. Zhang, T. Skeini, H. Richardson, J. Lee, and N. A. Kotov, Gold nanoparticle ensembles as heaters and actuators: melting and collective plasmon resonances, *Nanoscale Research Letters* **1**, 84 (2006).
- [33] J. Giddings, P. M. Shinudu, and S. N. Semenov, Thermophoresis of metal particles in a liquid, *Journal of Colloid and Interface Science* **176**, 454 (1995).
- [34] P. Gaspard and R. Kapral, The stochastic motion of self-thermophoretic janus particles, *Journal of Statistical Mechanics: Theory and Experiment* **2019**, 074001 (2019).
- [35] T. Bickel, G. Zecua, and A. Würger, Polarization of active janus particles, *Phys. Rev. E* **89**, 050303 (2014).
- [36] D. Hasselman and L. F. Johnson, Effective thermal conductivity of composites with interfacial thermal barrier resistance, *Journal of Composite Materials* **21**, 508 (1987), <https://doi.org/10.1177/002199838702100602>.
- [37] J. D. Olarte-Plata and F. Bresme, Orientation of janus particles under thermal fields: The role of internal mass anisotropy, *The Journal of Chemical Physics* **152**, 204902 (2020), <https://doi.org/10.1063/5.0008237>.
- [38] J. D. Olarte-Plata, J. Gabriel, P. Albella, and F. Bresme, Spatial control of heat flow at the nanoscale using janus particles, *ACS Nano* **16**, 694 (2022).
- [39] J. Muscatello, E. Chacón, P. Tarazona, and F. Bresme, Deconstructing temperature gradients across fluid interfaces: The structural origin of the thermal resistance of liquid-vapor interfaces, *Phys. Rev. Lett.* **119**, 045901 (2017).
- [40] M. Yang and M. Ripoll, Thermophoretically induced flow field around a colloidal particle, *Soft Matter* **9**, 4661 (2013).
- [41] D. B. Mayer, T. Franosch, C. Mast, and D. Braun, Thermophoresis beyond local thermodynamic equilibrium, *Phys. Rev. Lett.* **130**, 168202 (2023).